Palladium nanoparticles anchored on silanol nests of zeolite showed superior stability for methane combustion

Yingjie Wang [a,c,d,1], Yanwei Sun [a,b,1], Guangyan Xu [a,b,*], Zhi Liu [a,b], Wei Shi [a,b], Xiaoyan Shi [a,b], Yunbo Yu [a,b,c,d], Hong He [a,b,c,d,*]

[a] State Key Joint Laboratory of Environment Simulation and Pollution Control, Research Center for Eco-Environmental Sciences, Chinese Academy of Sciences, Beijing 100085, China
[b] University of Chinese Academy of Sciences, Beijing 100049, China
[c] Ganjiang Innovation Academy, Chinese Academy of Sciences, Ganzhou 341000, China
[d] School of Rare Earths, University of Science and Technology of China, Hefei 230026, China

ARTICLE INFO

ABSTRACT

Supported palladium catalysts exhibit exceptional catalytic activity in methane combustion, yet they still suffer from rapid deactivation due to sintering during reaction conditions. In this study, we reported supported palladium catalysts on siliceous MFI zeolite with abundant silanol nests, which served as highly effective anchoring sites for stabilizing PdOx nanoparticles. The innovative Pd/S-1-OH catalyst demonstrated remarkable catalytic activity in methane combustion, achieving a low T_{50} of 295 °C. Additionally, this catalyst demonstrated extremely high stability even after severe hydrothermal aging at 750 °C for 16 hours, and maintained long-term stability in wet methane combustion for 100 hours. Various characterizations confirmed the anchoring effect of silanol nests for PdOx nanoparticles, primarily attributed to the robust binding energy between PdOx nanoparticles and silanol nests. Furthermore, the engineering of silanol nests on zeolite through desilication significantly improved the stability of Pd/silicalite-1, thereby benefiting for the development of palladium/zeolite catalysts with exceptional stability.

1. Introduction

Catalyst sintering, a primary factor inducing the decline in catalytic activity and selectivity at elevated reaction temperatures, presents a formidable challenge within the domain of heterogeneous catalysis [1, 2]. A conspicuous instance involves the application of supported catalysts incorporating PdO as an active species, which are commonly employed for the abatement of low-concentration methane (CH₄) in natural gas vehicles exhaust [3–7]. Nonetheless, when exposed to high temperature and humidity environments in operational contexts, the Pd-based catalysts inevitably succumb to sintering [8,9]. The detrimental ramifications of this process can be assuaged through the meticulous engineering of the interaction of the catalytic active site with the support, underscoring the pivotal necessity of catalysts exhibiting strong metal-support effects capable in the stabilization and anchoring of PdOx nanoparticles in such demanding conditions [10–12].

Pd supported on alumina is one of the most effective methane oxidation catalyst (MOC) [13,14], and significant process has been made in refining and enhancing Pd/Al₂O₃ catalysts [10,14–19]. Aluminosilicate zeolites, a class of microporous crystalline solids, have shown promise in mitigating the adverse effect of water on methane combustion [20,21]. A suite of Pd-based MOC catalysts, exemplified by Pd/SSZ-39 and Pd/Na-MOR, characterized by commendable hydrothermal stability, has been developed [6,22]. However, conventional impregnation methodologies typically yield non-uniform and relatively substantial particles on the external surface. This has stimulated a burgeoning interest in the encapsulation of metal clusters or particles within zeolite matrices featuring small, stable, and uniform pores [23–27]. As an illustration, an encapsulated Pd@S-1 catalyst, wherein PdOx nanoparticles were confined within hydrophobic silicalite-1, was synthesized and manifested elevated stability in methane abatement [24,28]. Recently, we also reported a novel encapsulated Pd@S-2 catalyst

---

exhibiting superior catalytic activity and stability in the wet methane catalytic combustion under challenging conditions [29].

Despite advancements achieved through the preparation of catalysts employing metal encapsulation, particularly in enhancing the catalytic oxidation activity of methane and water resistance, the methane conversion rate experiences a substantial decline during prolonged steady-state experiments. In the context of high space velocity, high temperature, and high humidity, it becomes imperative to refine the metal-support interaction further. This refinement aims to ameliorate the catalyst's resistance to sintering, thereby bringing its performance into closer alignment with practical applications.

Generally, the structure of the zeolite framework has a minimal impact on the dispersion and stability of PdOx nanoparticles [30]. The primary factor that impacts the stability of PdOx nanoparticles is indeed lack of stable anchoring sites within the zeolite structure [31–33]. To address this issue, we synthesized a zeolite catalyst with PdOx nanoparticles anchored on a siliceous MFI zeolite with abundant silanol nests (Pd/S-1-OH, Figure S1) [34,35]. Compared with the encapsulated Pd@S-1 and commercial Pd/Al$_2$O$_3$ catalysts, Pd/S-1-OH with a large number of silanol nests demonstrated excellent activity and long-term stability in methane combustion. Various characterizations confirmed that the silanol nests exhibited a strong interaction with PdOx nanoparticles, effectively maintaining their stability even under harsh conditions of high temperature and humidity. Comprehensive comparative experiments, including both the removal and engineering of silanol nests, have confirmed the anchoring effect of silanol nests on PdOx nanoparticles. Our study presents a novel approach to enhance the sintering resistance of precious metals and paves the way for developing more efficient Pd-based catalysts for low-temperature methane combustion.

2. Experimental section

2.1. Catalyst Synthesis

Pd/S-1-OH was synthesized by an impregnation method using S-1-OH zeolite (Zhuoran Environmental Protection Co. Ltd) as support. Specifically, 0.27 mL of Tetraammine palladium (II) nitrate solution (10 wt% in H$_2$O, Sigma-Aldrich) was added into the deionized water containing 1 g S-1-OH zeolite. After stirring for 30 min, it was transferred to the rotary evaporator to remove water. The obtained sample was dried at 80 °C overnight, and calcined in air at 550 °C for 8 hours with a heating rate of 1 °C/min. For comparison, an encapsulated Pd@S-1 catalyst was synthesized by a hydrothermal method [24]. Besides, Pd/Al$_2$O$_3$, Pd/S-1-OH-800, Pd/S-1, and Pd/S-1-DS were prepared by the above impregnation method using Al$_2$O$_3$ (Sasol, SBA 200), S-1-OH-800, S-1, S-1-DS as supports, respectively. Specifically, the S-1-OH-800 zeolite was obtained by calcining the S-1-OH zeolite in air at 800 °C for 8 hours. The S-1 zeolite was synthesized using the aforementioned hydrothermal method [24], and subsequently, this zeolite underwent desiliconization in an alkali solution at high temperature to obtained the S-1-DS zeolite. The catalysts were further hydrothermally aged in a wet environment (10%H$_2$O/3.5%O$_2$/N$_2$) at 750 °C for 16 hours, and the resulting sample was designated as "catalyst-HTA". The detailed experimental information can be found in the Supporting Information.

2.2. Catalyst characterization

The physical properties of catalysts were investigated by N$_2$ adsorption-desorption, inductively coupled plasma optical emission spectrometry (ICP-OES), X-ray diffraction (XRD), high resolution-transmission electron microscopy (HR-TEM), high-angle annular dark field scanning transmission electron microscopy (HAADF-STEM), ^{1}H magic-angle-spinning (MAS) NMR, and Fourier Transform Infrared Spectrometer (FTIR). The chemical properties of these catalysts were investigated by H$_2$ temperature-programmed reduction (H$_2$-TPR), O$_2$

temperature-programmed decomposition (O$_2$-TPD), X-ray photoelectron spectroscopy (XPS), temperature-programmed reduction of CH$_4$ and temperature-programmed oxidation of O$_2$ (CH$_4$-TPR&O$_2$-TPO), and *in situ* Raman. The detailed experimental information can be found in the Supporting Information.

2.3. Evaluation of Catalytic Activity

The catalytic performance of the as-synthesized catalysts in methane combustion was evaluated at atmospheric pressure in a quartz fixed-bed reactor [29]. Before the experiment, all catalysts were pretreated at 650 °C in steam (10% H$_2$O in N$_2$) for 30 min. The reaction gas was composed of 0.1% CH$_4$, 3.5% O$_2$, 10% H$_2$O (if needed), and N$_2$ balance at a total flow of 1000 mL min^{-1}. 200 mg of catalyst (40–60 mesh) was used, corresponding to a weight hourly space velocity (WHSV) of 300, 000 mL g^{-1} h^{-1}. The concentration of CH$_4$ was monitored by an infrared spectrometer (Nicolet iS10).

$$CH_4 \text{ conversion} = \frac{[CH_4]_{in} - [CH_4]_{out}}{[CH_4]_{in}} \times 100\% \qquad (1)$$

Where $[CH_4]_{in}$ and $[CH_4]_{out}$ represent the inlet and outlet concentrations of CH$_4$, respectively.

During kinetic experiments, 20 mg catalyst was diluted with quartz sand at a ratio of 1:4 to minimize the exothermic effect of the reaction, and the effect of internal diffusion and external mass transfer resistances have been eliminated in our previous work [29]. The CH$_4$ conversion was kept below 20%, and the apparent activation energies were calculated using the Arrhenius equations and reaction rate (r) equations:

$$r = \frac{F_{CH_4} \times X_{CH_4}}{W_{Pd}} \qquad (2)$$

$$k = Ae^{\left(-\frac{Ea}{RT}\right)} \qquad (3)$$

Where r represents the reaction rate (μmol_{CH_4} g$_{Pd}^{-1}$ s^{-1}), k represents the reaction rate constant, F_{CH4} represents the CH$_4$ flow rate (mol_{CH4} s^{-1}), X_{CH4} denotes the conversion of CH$_4$ and W_{Pd} is the mass of the palladium species on the catalyst (g$_{Pd}$).

2.4. DFT Calculations

First-principles density functional theory (DFT) calculations were performed using the Vienna Ab initio Simulation Package (VASP) [36] with the projector augmented wave (PAW) method [37]. For simplification, a Pd$_{13}$O$_{20}$ cluster was used to simulate the PdOx nanoparticles. MFI (101) is loaded with a Pd$_{13}$O$_{20}$ cluster with lattice constants of a=24.083 and b=19.899. Three Si atoms close to each other on the surface were removed and hydrogenated to obtain the defect model. The adsorption energy (E$_{ads}$) was calculated as follow:

$$E_{ads} = E_{zeolite+PdO \, NPs} - E_{zeolite} - E_{PdO \, NPs} \qquad (4)$$

Where E$_{zeolite+PdO \, NPs}$, E$_{zeolite}$, and E$_{PdO \, NPs}$ refer to the free energies of the PdOx nanoparticles adsorbed on the zeolite, the zeolite, and the PdOx nanoparticles, respectively.

3. Results and discussion

3.1. Catalyst activity and stability

The catalytic performance of catalysts in the methane combustion reaction was conducted in an atmosphere similar to the practical conditions, which consisted of 0.1% CH$_4$, 3.5% O$_2$ and 0 or 10% H$_2$O, at an extremely high WHSV of 300,000 mL g^{-1} h^{-1} (Figs. 1a and 1b). For comparison, a state-of-the-art Pd/Al$_2$O$_3$ catalyst with similar Pd loading was used as a reference sample [3–5]. Additionally, an encapsulated
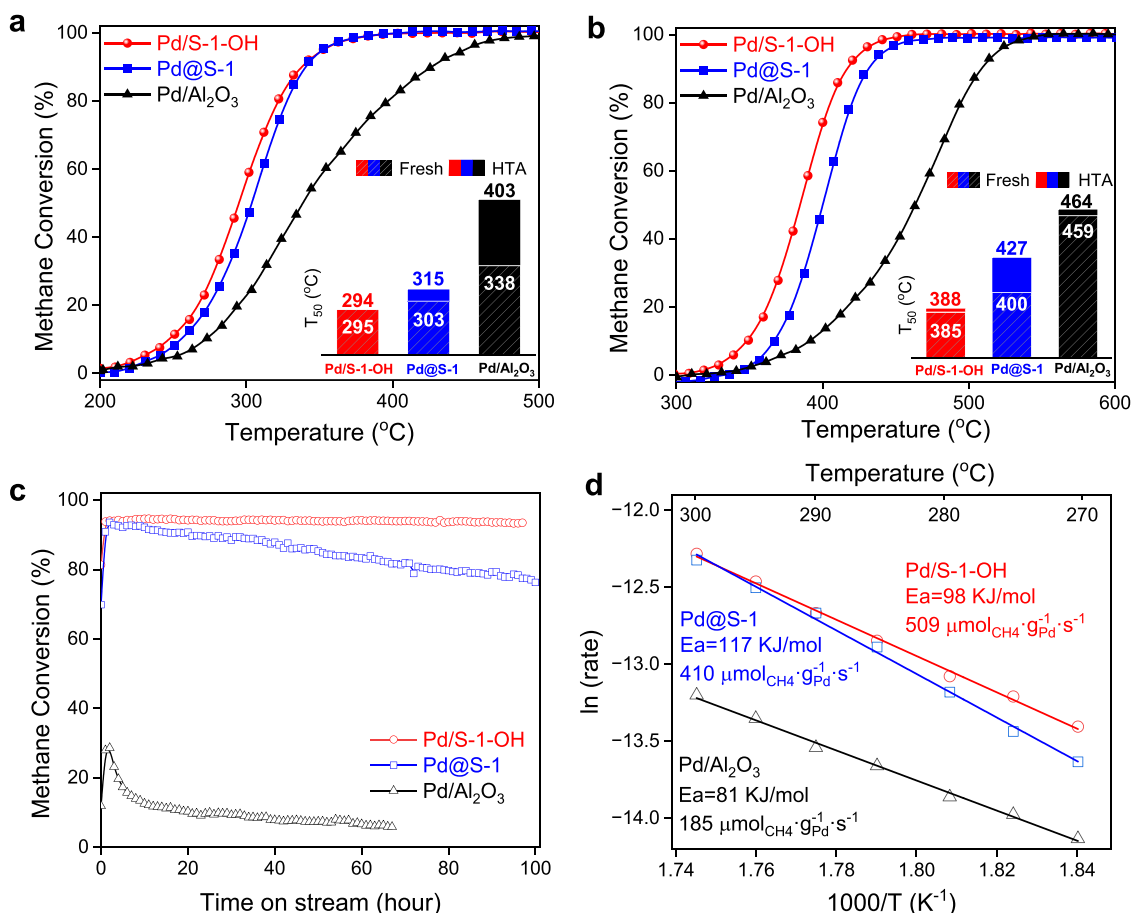
Fig. 1. The catalytic performance of palladium catalysts in (a) dry and (b) wet methane combustion, and inserted histogram shows the comparison of T_{50} between fresh and HTA samples. (c) Long-term stability test on palladium catalysts in wet methane combustion at 450 °C. (d) Arrhenius plots for methane combustion. Typical conditions: 0.1% CH_4, 3.5% O_2 and 10% H_2O (when added) in N_2 balance, WHSV=300,000 mL g^{-1} h^{-1}. Hydrothermal aging conditions: 750 °C for 16 hours with a gas mixture containing 10% H_2O/3.5%O_2/N_2.

Pd@S-1 catalyst with palladium nanoparticles confined inside the zeolite (S-1) with same MFI framework was prepared for comparison. Under dry conditions, the Pd/S-1-OH catalyst exhibited outstanding performance with a T_{50} (temperature at which 50% CH_4 conversion occurs) of 295 °C, slightly lower than that of the encapsulated Pd@S-1 catalyst (303 °C). While the Pd/Al$_2$O$_3$, the widely used catalyst, has the highest T_{50} of 338 °C. Similarly, under wet conditions, the Pd/S-1-OH catalyst demonstrated superior catalytic performance compared to the Pd/Al$_2$O$_3$ and Pd@S-1 catalysts, and the T_{50} of Pd/S-1-OH (385 °C) was 15 °C and 74 °C lower than that of Pd@S-1 (400 °C) and Pd/Al$_2$O$_3$ (459 °C), respectively [38–40]. To evaluate the sintering resistance of catalysts, they were further hydrothermally aged under harsh conditions (10% H$_2$O/3.5% O$_2$/N$_2$) at 750 °C for 16 hours [22], and the T_{50} of the HTA samples were shown in the histograms inserted in Figs. 1**a** and 1**b**. The results showed that the methane combustion performance of Pd/S-1-OH-HTA catalyst changed negligible (T_{50} =294 °C for dry condition and T_{50}=388 °C for wet condition), irrespective of the presence of water vapor, demonstrating to be one of the most highly efficient MOC catalysts (Table S1) [6,9,10,20,22,25,28, 41–46]. In contrast, Pd@S-1-HTA was deactivated to some extent after hydrothermal aging, with the T_{50} increases by 12 °C under dry condition and 27 °C under wet condition, respectively. Besides, a supported Pd catalyst (Pd/ZSM-5) on zeolite with the same MFI framework exhibited poor stability after hydrothermal aging (Figure S3). Notably, the activity of Pd/Al$_2$O$_3$-HTA was significantly suppressed, with the T_{50} increasing to 403 °C for dry condition and 464 °C for wet condition. Additionally, Pd/S-1-OH with different Pd contents demonstrated high performance

in methane combustion under practical conditions in a complex atmosphere consisting of 0.1% CH_4, 0.1% NO, 3.5% O_2, 6% CO_2, and 10% H_2O (Figures S4 and S5), Clearly, the Pd/S-1-OH catalysts possessed excellent activity and stability in methane combustion and outperformed the encapsulated Pd@S-1 and conventional Pd/Al$_2$O$_3$ catalysts (Figure S6).

Since the methane oxidation reaction is highly exothermic, the catalysts usually suffer from deactivation by the sintering of the active component during long-term operation.[47] Long-term stability test demonstrated that the Pd/S-1-OH catalyst exhibited a high efficiency of 94% for wet methane combustion at 450 °C for nearly 100 hours (Fig. 1**c**). By contrast, the methane conversion rate on the encapsulated Pd@S-1 catalyst decreased from 93% to 77% over the same period. On the supported Pd/Al$_2$O$_3$ catalyst, methane conversion decreased rapidly from 27% to 11% at 450 °C in the first 5 hours, followed by further gradual deactivation. This phenomenon is related to the initial formation of inactive Pd(OH)$_2$ species through the reaction between water vapor and PdOx species (PdO + H$_2$O = Pd(OH)$_2$) within the first few hours [47–49], followed by a gradual degradation involving extensive sintering of palladium in the presence of steam.

The apparent activation energies of methane oxidation over Pd-based catalysts were measured in a kinetic-controlled region. The results showed that the activation energies of the Pd/S-1-OH and Pd/S-1-OH-HTA were 98 kJ mol^{-1} and 108 kJ mol^{-1}, respectively (Fig. 1**d** and S7 and Table S2). In addition, the activation energy of Pd/Al$_2$O$_3$ was 81 kJ mol^{-1} and 104 kJ mol^{-1} for fresh and HTA samples, respectively, which were consistent with those reported in previous literatures [50].

Whereas, the activation energies of Pd@S-1 and Pd@S-1-HTA were as high as 117 kJ mol^{-1} and 112 kJ mol^{-1}, respectively. Furthermore, both Pd/S-1-OH (509 μmol_{CH_4} g_{Pd}^{-1} s^{-1}) and Pd/S-1-OH-HTA (410 μmol_{CH_4} g_{Pd}^{-1} s^{-1}) achieved high reaction rates during methane combustion at 300 °C surpassing the performance of Pd/Al$_2$O$_3$ and Pd@S-1, demonstrating to be one of the most efficient MOC catalysts [29]. These findings demonstrate the exceptional catalytic performance and remarkable stability of the novel Pd/S-1-OH catalyst in methane combustion reactions.

3.2. Catalyst characterizations

The Pd-based catalysts were systematically characterized by various techniques. X-ray diffraction (XRD) pattern analysis confirmed the presence of the typical MFI structure on both the Pd/S-1-OH and Pd@S-1 catalysts, while no obvious Pd signal was observed in both catalysts, proving that the well distribution of Pd species. In contrast, the diffraction peaks attributed to the (101) plane of PdO (2θ = 33.8°, PDF: 00–043–1024) was found on Pd/Al$_2$O$_3$ catalyst (Figure S8). After hydrothermal aging, XRD pattern revealed hydrothermal aging did not affect the structure and crystallinity of the zeolite catalysts. In contrast, hydrothermal aging resulted in a slight enhancement of the crystalline phase of PdO (101) on Pd/Al$_2$O$_3$, as evidenced by calculation using the Scherrer's formula (Table S3), indicating the sintering of Pd species on this sample.

Additionally, nitrogen adsorption measurements showed a type I adsorption-desorption isotherm on the Pd/S-1-OH and Pd@S-1 catalysts, which was consistent with typical microporous materials. The Pd/S-1-OH and Pd@S-1 catalysts possessed large specific surface areas of 304 m^2/g and 421 m^2/g, respectively, which were much higher than that on the Pd/Al$_2$O$_3$ (198 m^2/g) (Figure S9 and Table S4). After hydrothermal aging, the specific surface area of these three catalysts decreased to some extent. Additionally, Pd/S-1-OH also possessed an external surface area of 169 m^2/g, which remained unchanged after hydrothermal aging. ICP-OES analysis demonstrated that the Pd content in these three samples was approximately 1.0 wt% (Table S4).

The HAADF-STEM images showed that Pd/S-1-OH was rod-like, with an average diameter of about 150 nm. The PdOx nanoparticles were strikingly uniform and well-ordered dispersed on the surface of Pd/S-1-OH zeolite, primarily concentrated along the edges, with an average particle size of 7.1 nm (Fig. 2a and S10). The locally detailed structure (Fig. 2b) depicted palladium nanoparticles were anchored on the surface of zeolite, with half of them buried inside. Notably, the predominant crystal face was identified as PdO(101), which is known to be the primary crystal face involved in the methane oxidation reaction [51]. Impressively, even after undergoing hydrothermal aging, the palladium nanoparticles (7.6 nm) remained orderly dispersed, and no obvious sintering was observed (Figs. 2c, 2d and S11).

The Pd@S-1 has a typical hexagonal cubic shape with an average crystal size of about 300 nm, and palladium nanoparticles were well dispersed insides the zeolite with an average particle size of 3.2 nm, consistent with the literature (Fig. 2e and S12) [24,25]. Moreover, hydrothermal aging resulted in obvious sintering of PdOx nanoparticles on Pd@S-1-HTA, with the average sizes increasing to 4.7 nm (Fig. 2f and S13). The distribution of Pd nanoparticles (7.6 nm) on the Pd/Al$_2$O$_3$ was non-uniform, and the particle size increased to 10.8 nm after hydrothermal aging (Figures S14 and S15), which might be responsible for its poor catalytic performance in methane oxidation.

XPS analysis was conducted to investigate the valence state of active components on these catalysts. The Pd 3d$_{5/2}$ spectra was deconvoluted into two peaks centered at about 337.0 and 342.0 eV, which could be assigned to Pd^{2+} and Pd^{4+} species, respectively. On the Pd/S-1-OH and Pd/Al$_2$O$_3$, the Pd species mainly presented as Pd^{2+} state on these catalysts, accounting for 90% and 84%, respectively (Fig. 3a and S16) [10, 52]. After hydrothermal aging, the XPS signal slightly decreased on the Pd/S-1-OH-HTA, possibly indicating a decrease in the oxidized Pd
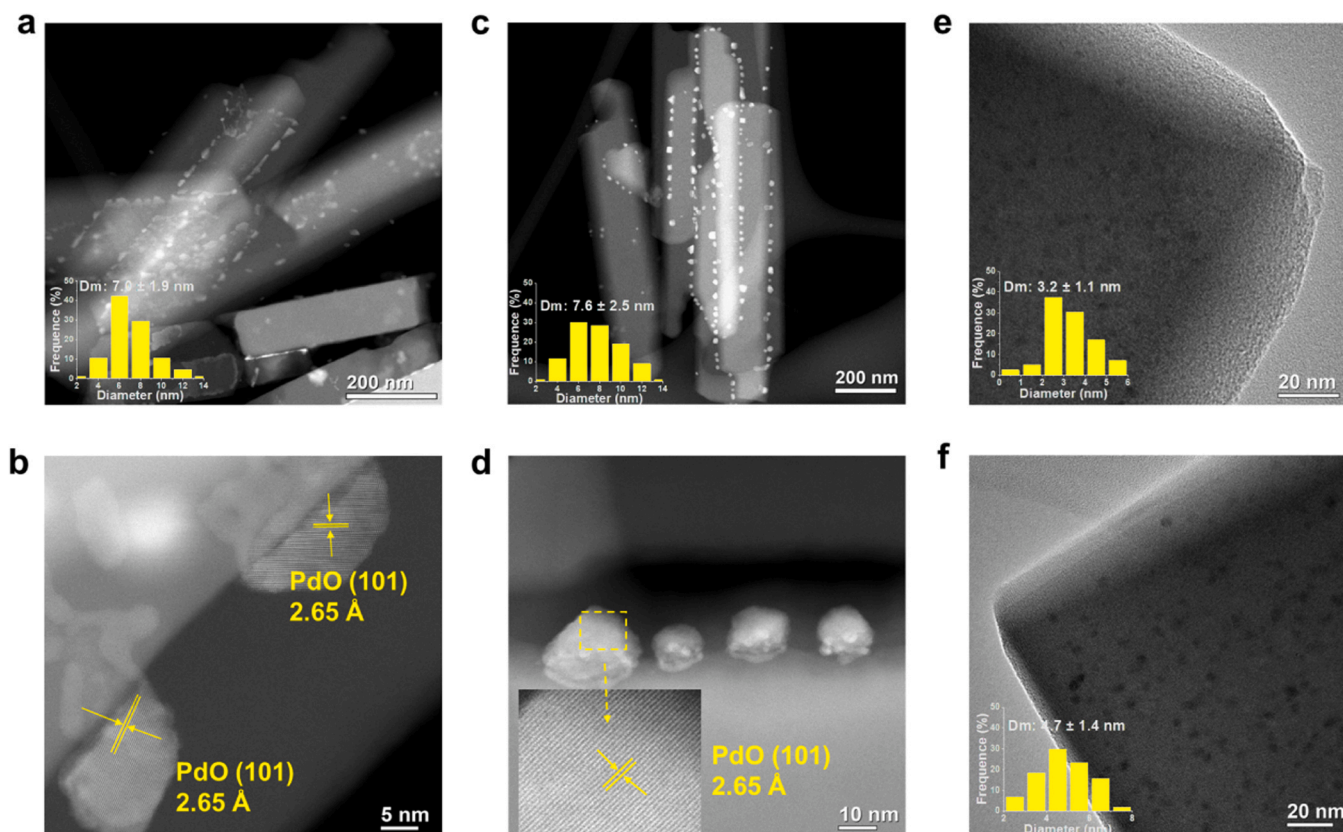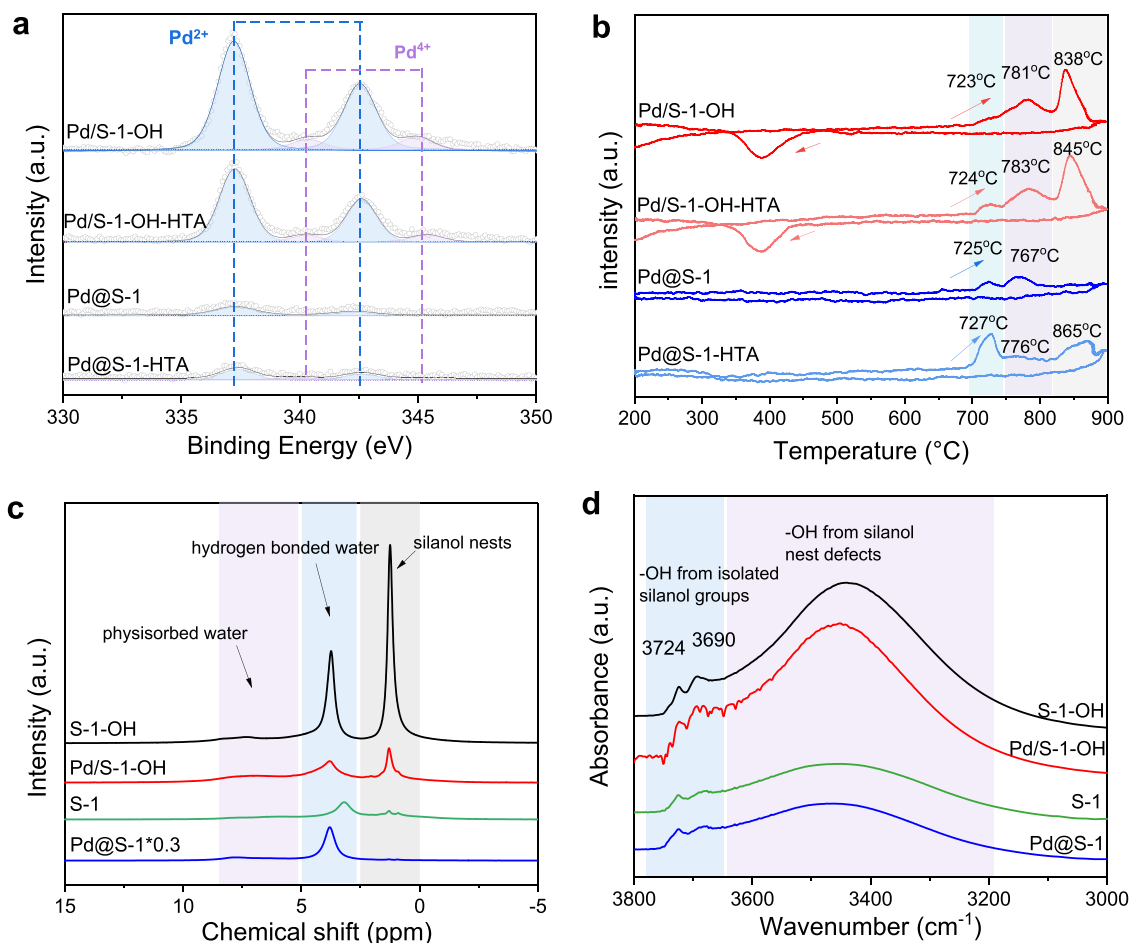

Fig. 2. HAADF-STEM images of (a, b) Pd/S-1-OH and (c, d) Pd/S-1-OH-HTA. HR-TEM images of (e) Pd@S-1 and (f) Pd@S-1-HTA.

Fig. 3. (a) XPS results and (b) O_2-TPD profiles of fresh and hydrothermal aged catalysts; (c) ^{1}H MAS NMR spectra of catalysts; (d) FT-IR spectra in the OH stretching vibration region of catalysts.

species (as confirmed by the subsequent H_2-TPR experiment). Similarly, the decreased XPS signal for Pd species on the Pd/Al$_2$O$_3$-HTA could be related to the change in the particle size of PdOx nanoparticles and the decrease in oxidized Pd species. Conversely, no discernible XPS peaks were observed over Pd@S-1, primarily due to the confinement of PdOx within the zeolite structure [28]. The minor increase in the XPS signal of Pd@S-1-HTA may be attributed to the simultaneous sintering of PdOx nanoparticles and their migration to shallow interior of zeolite crystals from deep inside [53,54]. Notably, hydrothermal aging hardly affected the valance state of Pd species on these Pd-based catalyst. The XPS spectra of O 1 s orbitals in Pd-based catalysts were deconvoluted into two characteristic peaks (Figures S16 and S17), corresponding to lattice oxygen (O$_{latt}$) at 531.0 eV and surface chemisorbed oxygen (O$_{surf}$) at 532.3 eV. Across these samples, oxygen species were predominantly in the form of lattice oxygen, and hydrothermal aging did not impact the composition and proportion of oxygen species.

To investigate the reducibility of these MOC catalysts, H_2-TPR measurements were carried out. The low-temperature desorption peaks below -20 °C was associated with the desorption of Ar from the zeolite (Figure S18) [54,55], and the H_2 consumption peak at about 10 °C correspond to the reduction of PdOx species [54]. For Pd/S-1-OH, the reduction peak of PdOx on both fresh and HTA samples were at 13 °C, indicating that hydrothermal aging did not significantly affect the reducibility of PdOx. Furthermore, the sharpening of the H_2 consumption peak might be attributed to the homogeneous redispersion of PdOx nanoparticles induced by high-temperature steam, while the slight decrease in H_2 consumption may be attributed to the formation of metallic Pd species under hydrothermal aging conditions [40]. In

contrast, the reduction peak on Pd@S-1 increased from 7 °C to 15 °C after hydrothermal aging, indicating the suppression of hydrothermal aging on this sample. Similarly, the reduction peak on Pd/Al$_2$O$_3$ also shifted to higher temperature after hydrothermal aging. Besides, a new peak at 25 °C emerged on the Pd/Al$_2$O$_3$-HTA, suggesting the formation of large PdO nanoparticles [56]. A negative peak was observed between 69 and 85 °C on all samples, which was attributed to the decomposition of PdHx species [57].

The stability of PdOx species on these catalysts were further evaluated by O_2-TPD experiments (Fig. 3b). Prior to the O_2-TPD experiments, the catalysts underwent a heating pretreatment from 200 °C to 900 °C to eliminate the effects of the supports [13]. During the heating process, O_2-release peaks for all the samples appeared in the range of 600–900 °C, attributed to the decomposition of PdOx species to form metallic Pd species. Subsequently, this species could be re-oxidized to form PdOx species during the cooling process, giving rise to a negative peak at 300–550 °C [58]. On the Pd/S-1-OH, three decomposition peaks were observed, attributing to the decomposition of surface PdOx species ($\sim$720 °C), subsurface PdOx (780 °C), and bulk PdOx (840 °C), respectively [13,59,60]. After hydrothermal aging, these three peaks remained unchanged, indicating that PdOx in Pd/S-1-OH maintained a high stability, suggesting a strong metal-support interaction on Pd/S-1-OH. Such metal-support interaction suppressed the decomposition and sintering of PdOx nanoparticles, which further contributed to the excellent hydrothermal stability of the Pd/S-1-OH catalysts. In contrast, the decomposition temperatures of PdOx on the Pd@S-1 catalysts were slightly lower than that on the Pd/S-1-OH catalysts. In Pd@S-1-HTA, the low-temperature peak attributed to the

decomposition of surface PdOx species was enhanced slightly, indicating that PdOx species migrated to the shallow interior of zeolite crystals, which was consistent with XPS analysis. Notably, the PdOx species on the Pd/Al$_2$O$_3$ was extremely unstable, with a low decomposition temperature of ~610 °C, thus resulting in poor stability in methane combustion (Figure S19). Additionally, hydrothermal aging induced the formation of some metallic Pd species and bulk PdOx, leading to decreased O$_2$ desorption and a higher decomposition temperature (865 °C).

The differences between the support structures could be identified by the ^{1}H NMR and OH stretching vibration band of FT-IR spectroscopy (Figs. 3c and 3d). The ^{1}H MAS NMR spectra revealed that there were physical adsorbed H$_2$O (~ 7 ppm) and hydrogen bonded H$_2$O (~ 4 ppm) signals on Pd/zeolite catalyst. In contrast to S-1-OH and Pd/S-1-OH samples, there were no silanol nests (~ 1.2 ppm) on the S-1 and Pd@S-1 (Fig. 3c) [34,61,62]. Additionally, the anchoring of PdOx species in Pd@S-1 was achieved via the confinement effect of zeolite pores, rather than relying on silanol nests. Furthermore, FT-IR spectra show that two sharp bands (3690 and 3725 cm^{-1}) assigned to OH stretching vibrations from isolated external silanol groups were observed on the zeolite catalysts. Besides, a broad band (3200–3650 cm^{-1}) attributed to hydrogen-bonded silanol groups was also observed on the S-1-OH and Pd/S-1-OH, further verified the presence of abundant -OH species of silanol nest on this sample (Fig. 3d) [63–65]. Comparison to the Pd@S-1 catalyst, the higher abundance of silanol nests on S-1-OH suggested their beneficial role in anchoring PdOx nanoparticles.

3.3. Reaction mechanism

Combined CH$_4$-TPR and O$_2$-TPO were employed to explore the activation of CH$_4$ and O$_2$ (Figs. 4a, 4b and S20), corresponding to the reduction of PdOx species by CH$_4$ and the re-oxidation of reduced Pd species by O$_2$ in methane combustion on Pd-based catalysts, respectively

[40]. During CH$_4$-TPR experiment, the methane consumption peak could be observed in all fresh samples at about 260–270 °C, accompanied by the generation of CO$_2$ and H$_2$O concurrently. Among them, the Pd/S-1-OH exhibited the most remarkable ability to activate methane at a low temperature (264 °C), lower than that on Pd@S-1 (271 °C) and Pd/Al$_2$O$_3$ (272 °C), highly consistent with the light-off performance of these catalysts. Notably, little H$_2$O was observed on Pd/Al$_2$O$_3$ at temperatures below 350 °C, possibly due to H$_2$O adsorption on Al$_2$O$_3$, which would further suppress the low-temperature catalytic activity. After hydrothermal aging, the methane activation temperature followed the same order on Pd/S-1-OH-HTA (278 °C), Pd@S-1-HTA (279 °C), and Pd/Al$_2$O$_3$-HTA (285 °C), respectively (Figure S20). As the temperature further increased above 300 °C, the methane concentration continued to decline due to the occurrence of methane cracking, accompanied by the production of H$_2$. Besides, the cracking reaction on the Pd/Al$_2$O$_3$ catalysts was more intense than that on the Pd/S-1-OH and Pd@S-1 catalysts. During O$_2$-TPO experiment, O$_2$ consumption was observed at 315–335 °C on these samples, attributing to the re-oxidation of metallic Pd species. Similarly, the Pd species on Pd/S-1-OH were re-oxidized at a lower temperature (314 °C), whereas the re-oxidation of Pd species required higher temperatures on Pd@S-1 (325 °C) and Pd/Al$_2$O$_3$ (336 °C). In the hydrothermal aged samples, the re-oxidation of Pd species followed the same order on Pd/S-1-OH-HTA (321 °C), Pd@S-1-HTA (323 °C), and Pd/Al$_2$O$_3$-HTA (328 °C), respectively (Figure S20). Based on the CH$_4$-TPR and O$_2$-TPO results, Pd/S-1-OH demonstrated the best redox properties in methane combustion. Overall, the redox properties correlated with their catalytic activity, while other factors such as hydrophobicity also influence their catalytic performance in practical reactions.

In situ Raman experiments were performed to further investigate the involvement of PdOx species on Pd/S-1-OH in methane catalytic combustion (Figs. 4c-4f, S21). The Raman spectra shows the bands associated with the characteristic vibrations of the MFI zeolite framework
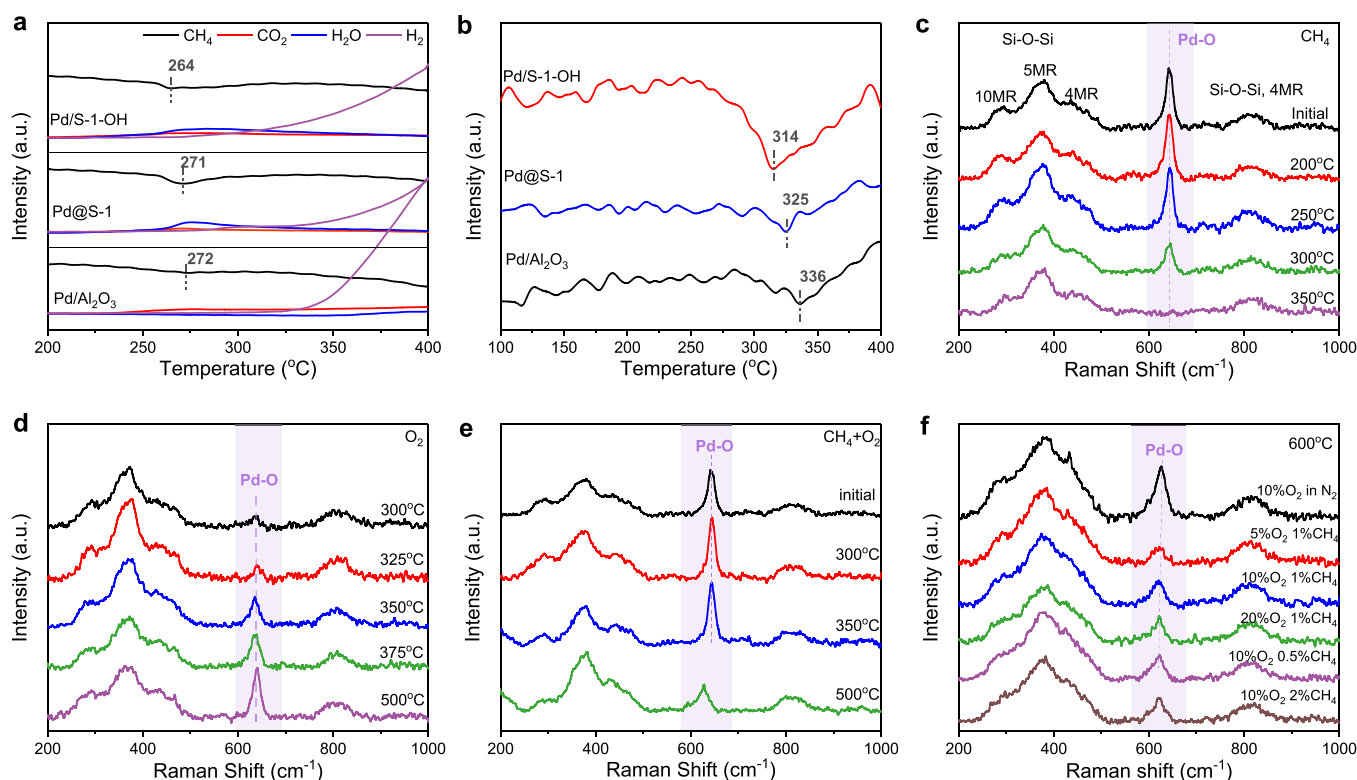
Fig. 4. (a) CH$_4$-TPR and (b) O$_2$-TPO profiles of catalysts. *In situ* Raman spectra of Pd/S-1-OH in an atmosphere containing (c) 1%CH$_4$ in N$_2$ and (d) 10% O$_2$ in N$_2$ at different temperatures. (e) *In situ* Raman spectra of Pd/S-1-OH in 1% CH$_4$ + 10% O$_2$ with temperature variation. (f) *In situ* Raman spectra of Pd/S-1-OH in different methane and oxygen concentrations at 600 °C.

(291 cm^{-1} for 10 R, 380 cm^{-1} for 5 R, and 437 cm^{-1} and 803 cm^{-1} for the 4 R units in the crystal phase) [66–68]. Additionally, the band at 660 cm^{-1} was ascribed to the vibration of Pd-O bond [66,69]. In the flow of CH$_4$/N$_2$, the band (660 cm^{-1}) for Pd-O bond was gradually vanished at temperatures above 300 °C, indicating the reduction of PdOx by CH$_4$, which was consistent with the results of CH$_4$-TPR. Besides, the signal for Pd-O bond was reappeared in the flow of O$_2$/N$_2$ at slightly higher temperatures (~350 °C), indicating the re-oxidation of Pd species (Figs. 4c and 4d) [66,69]. During steady-state methane combustion, the Pd species on the Pd/S-1-OH mainly existed in an oxidized state at low temperatures until at a high temperature of 500 °C (Fig. 4e). Moreover, at elevated temperatures, the concentration of reactants (CH$_4$ and O$_2$) significantly influenced the oxidized state of PdOx species, highlighting its high reactivity in methane combustion (Fig. 4f and S21).

3.4. Effect of silanol nests

To further verify the anchoring effect of zeolite silanol nests on PdOx nanoparticles, the silanol nests on S-1-OH were eliminated through high-temperature (800 °C) calcination (Figure S22), and the resulting catalyst loaded with Pd was named Pd/S-1-OH-800 [70]. High-temperature calcination induced the formation of twisted Si-O-Si bridges, thus removing the silanol defects on the S-1-OH zeolites (Figure S22) [71]. On the S-1-OH-800 zeolite, the peak of representing silanol nests (~1.2 ppm) in ^{1}H NMR was almost disappeared

(Figure S23), and the OH stretch region (3200–3650 cm^{-1}) in FT-IR was almost flat (Figure S24), confirming the elimination of silanol nests. After loading Pd, the signal representing silanol nests in ^{1}H NMR of Pd/S-1-OH decreased to some extent, suggesting the occupation of silanol nests by PdOx nanoparticles, while the peak of Pd/S-1-OH-800 remained unchanged (Fig. 5c). Moreover, HR-TEM showed that, different from the Pd/S-1-OH, Pd species were highly dispersed inside the Pd/S-1-OH-800 (Fig. 5a and S25), possibly facilitated by the weak interaction with Pd-O-Si sites. Such weak interaction, on one hand, induced the uniform dispersion of Pd species during the preparation process, and on the other hand, resulted in the sintering of Pd species during high-temperature aging (Fig. 5b and S26). Compared with Pd/S-1-OH, the methane oxidation activity of Pd/S-1-OH-800 decreased, with an increase in the T$_{50}$ from 385 °C to 403 °C (Fig. 5d).

In order to verify its stability, the catalysts were subjected to hydrothermal aging under the same conditions as previously mentioned. and hydrothermal aging induced a severe sintering of Pd species on the Pd/S-1-OH-800-HTA (17.9 nm) (Fig. 5b and S26). Consequently, the catalytic performance of Pd/S-1-OH-800-HTA decreased significantly compared to that of Pd/S-1-OH-800, with the T$_{50}$ value rising from 403 °C to 452 °C (Fig. 5d). The difference in T$_{50}$ value (ΔT$_{50}$) between fresh and HTA samples significantly increased from 3 °C on the Pd/S-1-OH to 49 °C on the Pd/S-1-OH-800 (Figure S27). Furthermore, the uniform or even monodisperse state of Pd species in Pd/S-1-OH-800 and its poor sintering resistance could be attributed to the absence of silanol nests on
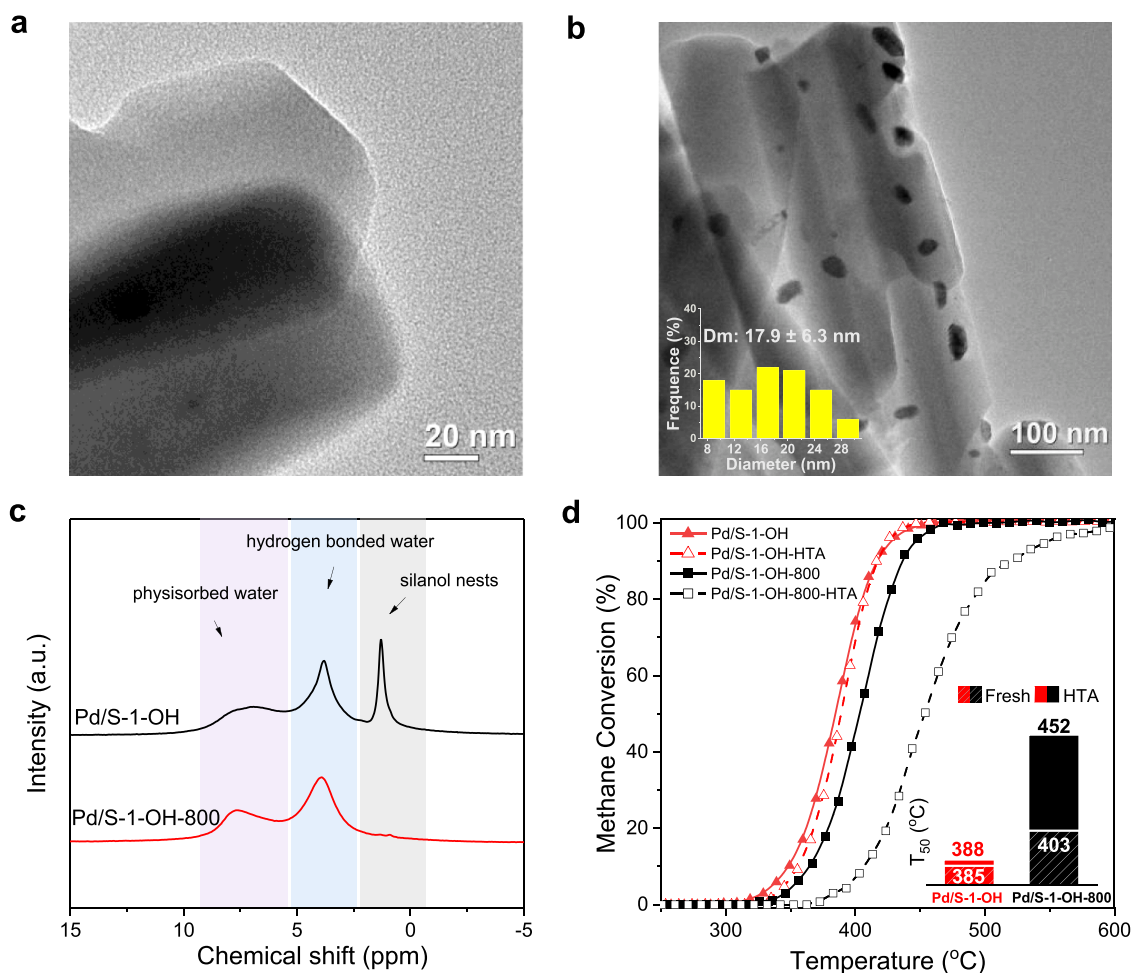
Fig. 5. HR-TEM images of (a) Pd/S-1-OH-800 and (b)Pd/S-1-OH-800-HTA. (c) ^{1}H NMR spectra of Pd/S-1-OH and Pd/S-1-OH-800 catalysts. (d) The catalytic performance of palladium catalysts in wet methane combustion, and inserted histogram shows the comparison of T$_{50}$ between fresh and HTA samples. Typical conditions: 0.1% CH$_4$, 3.5% O$_2$ and 10% H$_2$O in N$_2$ balance, WHSV=300,000 mL g^{-1} h^{-1}. Hydrothermal aging conditions: 750 °C for 16 hours with a gas mixture containing 10% H$_2$O/3.5%O$_2$/N$_2$.

the S-1-OH-800. The lack of silanol nests resulted in the migration and aggregation of PdOx clusters under high-temperature and hydrothermal conditions.

Moreover, a silicalite-1 zeolite without any inherent silanol nests was synthesized using the hydrothermal method and denoted as Pd/S-1 after Pd loading. Subsequently, the S-1 support underwent desilication to introduce silanol nests for comparison, and it was designated as Pd/S-1-DS [34]. On the S-1 zeolite, both FT-IR and ^{1}H NMR analysis confirmed the absence of silanol nests (Fig. 6, **S28** and **S29**). After desilication, the signal (3440 cm^{-1}) due to the silanol nests was significantly increased on the S-1-DS, indicating the generation of silanol nests on this sample (Figure S29). Desilication led to the removal of one or more units of the zeolite framework (SiO$_4$), resulting in the loss of structural integrity. To maintain stoichiometric equilibrium, these vacant microcavities were filled with -OH groups. The proximity of these groups facilitates the formation of numerous hydroxyl chains connected by hydrogen bonds, thus creating silanol defects [72]. After desilication, a certain amount of silanol nests were formed on the S-1-DS, as confirmed by FT-IR and ^{1}H NMR (Fig. 6, **S28** and **S29**). Due to the introduction of Pd, ^{1}H NMR spectra showed that the peaks were split into double peaks on the Pd/S-1-DS. HR-TEM image revealed Pd species in the form of PdOx nanoparticles with different particle sizes on the Pd/S-1 (3.2 nm) and Pd/S-1-DS (7.1 nm) (Figures S30 and S31), thus resulting in the different methane combustion activity (Fig. 6d). Compared to Pd/S-1-OH, the small PdOx nanoparticles on Pd/S-1 showed poor catalytic activity in methane combustion, possibly due to their particle sizes, heterogeneous distribution, and chemical states. In contrast, the Pd/S-1-DS, featuring a substantial number of silanol nests, demonstrated enhanced catalytic activity compared to Pd/S-1, with a T$_{50}$ that was 63 °C lower than the latter sample. Besides, the inferior catalytic performance of Pd/S-1-DS compared to Pd/S-1-OH might be due to difference in the properties of silanol nests and the framework of S-1-DS zeolite. Further optimization of the desilication conditions and the preparation methods may lead to improvements in the catalytic performance of this catalyst in methane combustion.

After hydrothermal aging, the PdOx nanoparticles on Pd/S-1-HTA underwent severe sintering, reaching a size of 18.7 nm (Fig. 6a and **S32**), whereas the PdOx nanoparticles on Pd/S-1-DS-HTA remained stable, exhibiting only a slight increase in particle size from 7.1 nm to 8.4 nm (Fig. 6b and **S33**). Consequently, the Pd/S-1-HTA was completely deactivated in methane combustion (Fig. 6d), while the Pd/S-1-DS-HTA demonstrated much better activity after hydrothermal aging, achieving a T$_{50}$ of 542 °C (Fig. 6d). The difference in T$_{50}$ value (ΔT$_{50}$) between the fresh and HTA samples significantly reduced from >300 °C on the Pd/S-1–109 °C on the Pd/S-1-DS (Figures S34 and S35). Besides, the desilication process of Pd/S-1 could potentially damage the framework of S-1 zeolite (Figure S36), leading to a minor reduction in methane combustion activity. The above results clearly demonstrated the critical role of silanol nests in anchoring and maintaining the stability of PdOx nanoparticles on these zeolite catalysts.

DFT calculations were further conducted to investigate the anchoring mechanism of silanol nests for PdOx nanoparticles [73,74]. Two surface models of S-1 zeolite were constructed, with the former model having a defect structure featuring three missing -SiO$_4^{4-}$ units
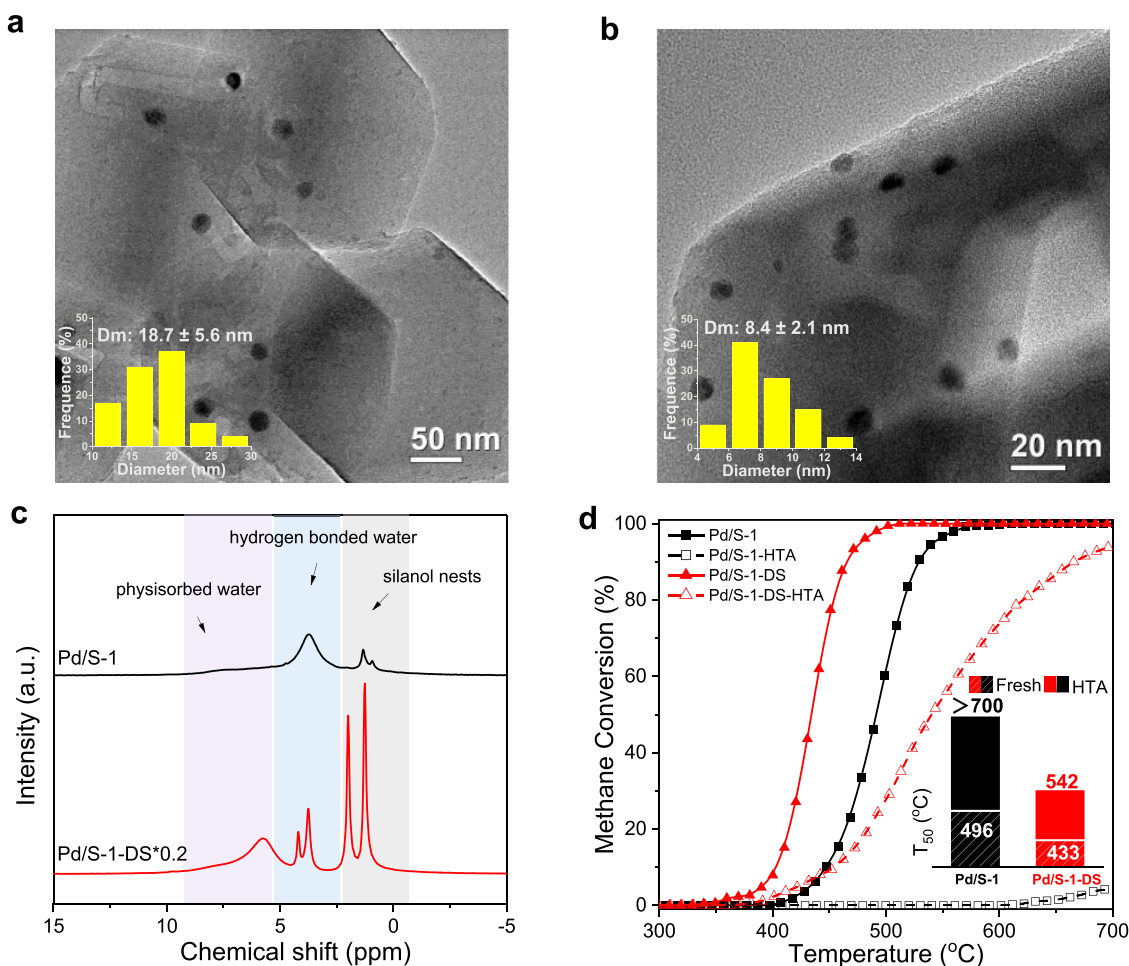
Fig. 6. HR-TEM images of (a) Pd/S-1-HTA and (b) Pd/S-1-DS-HTA. (c) ^{1}H NMR spectra of Pd/S-1 and Pd/S-1-DS catalysts. (d) The catalytic performance of palladium catalysts in wet methane combustion, and inserted histogram shows the comparison of T$_{50}$ between fresh and HTA samples.

(Figure S37) [34]. For simplification, a $Pd_{13}O_{20}$ cluster was used to simulate the PdO*x* nanoparticles [51,75–77]. The DFT calculations demonstrated that the PdO*x* nanoparticle was strongly bound to the hydroxylated surface, mainly through hydrogen bonds (represented by dashed lines), exhibiting a significant adsorption energy of −6.16 eV (Fig. 7a, S38 and S39). According to Bader charge analysis, the electron transfer between the PdO*x* cluster and adjacent framework oxygen within the silanol nests, owing to the formation of chemical bonds, amounted to 2.553 electrons (Figure S40). This value was lower than the electron transfer observed between the PdO*x* nanoparticles and the pristine S-1 surface (2.883 electrons), possibly due to the presence of hydrogen bonds. Consequently, the anchoring effect of silanol nests on PdO*x* clusters within zeolite is primarily attributed to hydrogen bonding, which enhances the stability of the PdO*x* nanoparticles.

3.5. Discussion

Generally, PdO*x* is recognized as the active component in the methane combustion reaction, and there exists a volcano-shaped correlation between the dimensions of palladium nanoparticles and their activity in methane combustion. Notably, size-specific high activity was obtained at 4–8 nm [14]. Consequently, meticulous control over the size and stabilization of palladium nanoparticles emerges as a paramount consideration for efficient methane combustion reactions. The key factor influencing the stability of PdO*x* nanoparticles is the presence of effective and stable anchoring sites within the zeolite structure. In the present work, Pd/S-1-OH catalyst was prepared by anchoring PdO*x* nanoparticles on a siliceous MFI zeolite with abundant silanol nests. The presence of silanol nests on the surface of S-1-OH zeolite with a large external surface area, especially at the edges of the zeolite, offers favorable sites for anchoring PdO*x* nanoparticles through hydrogen bonding. These silanol nests could remain stable until at high temperatures above 800 °C, thus contributing to the excellent hydrothermal stability of Pd/S-1-OH. PdO*x* nanoparticles anchored by silanol nests maintained an average particle size of 7 nm, exhibiting high activity in methane combustion [14]. In contrast, the palladium nanoparticles on the supported Pd/Al₂O₃ underwent easy sintering during the hydrothermal aging process.

Generally, two processes induce the sintering of metal nanoparticles: coalescence and Ostwald ripening [1]. On Pd/S-1, the coalescence process possibly occurred during hydrothermal aging, leading to significant sintering of PdO*x* nanoparticles. In contrast, on Pd/S-1-OH, Pd atoms were likely trapped by silanol nests to form PdO*x* nanoparticles during the preparation procedures, and the strong interaction between silanol nests and PdO*x* nanoparticles further maintained their stability during hydrothermal aging [78]. Overall, the presence of silanol nests in anchoring PdO*x* nanoparticles offers several advantages, including uniform dispersion, protection against sintering, and enhanced catalytic

activity. Besides, other factors such as crystal phase, chemical state, and hydrophobicity, also play significant roles in influencing the catalytic performance of palladium catalysts in methane combustion. For instance, surface OH groups on zeolites and oxides are essential in metal-support interaction [35,79], which enhances the stability of metal nanoparticles. However, they also tend to adsorb H_2O molecules, which can moisten PdO*x* to form Pd(OH)₂, thus leading to a decrease in catalytic activity.

Silanol nests are essentially hydrogen bonding groups produced by multiple closely spaced Si-OH in zeolite crystals, arising from vacancies in the crystal structure due to the absence of one or more T-O-T bonds, typically consisting of pairs or triads of $\equiv$SiO⁻...HO-Si$\equiv$ species [80,81]. Their formation results from (i) different synthetic methodologies and the nature and purity of the reagents and (ii) post-synthesis treatments of zeolites, such as alkali etching as discussed in this paper [34]. Additionally, various types of silanol nests, including geminal, vicinal, and bridged silanol, were also observed on zeolites, which could also serve as anchoring sites for metal nanoparticles [34]. The presence and stability of silanol nests provide a significant advantage in the dispersion and anchoring of active components. Recently, Ryoo et al. [33] reported that silanol nests in mesoporous zeolites could effectively activate hard-to-reduce rare earth elements, facilitating the formation of alloy nanoparticles, which hold great application prospects in the petrochemical process. Additionally, some research has also indicated a synergistic effect between silanol nests and other active sites in the vicinity. For example, Xiao et al. [35] found that silanol nests in zeolite could enrich the olefins to adjacent Rhodium nanoparticles, enhancing hydroformylation in toluene. The present work confirms the critical role of silanol nests in anchoring noble metal nanoparticles, representing a significant advancement in anti-sintering mechanisms. However, maintaining the stability of Pd/zeolite catalysts at ultrahigh temperatures remains a challenge, necessitating further regulation and improvement of silanol nest properties [80,82,83]. Future work should, therefore, focus on further exploring accurate regulation of the content, types (geminal, vicinal, bridged, and cluster types), and properties of silanol nests and their effect on the anchoring of PdO*x* nanoparticles, contributing to the development of more stable and efficient heterogeneous catalysts.

4. Conclusion

In conclusion, a supported palladium catalysts on siliceous MFI zeolite with abundant silanol nests was prepared and applied in methane combustion. The innovative Pd/S-1-OH catalyst exhibited remarkable catalytic activity, achieving a low T_{50} of 295 °C on both fresh and aged samples. Additionally, this catalyst demonstrated exceptional stability even after severe hydrothermal aging at 750 °C for 16 hours and maintained long-term stability in wet methane combustion for
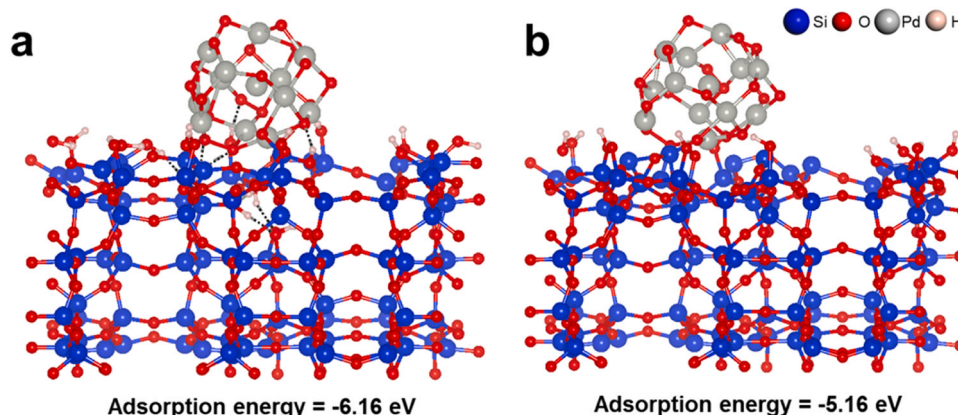

Fig. 7. Calculated adsorption energies of the PdO*x* nanoparticles on (a) silanol nests-containing S-1-OH and (b) S-1 zeolite.

100 hours. The experiments involving the destruction of silanol nests through high-temperature calcination and the creation of silanol nests through desilication unambiguously demonstrated the pivotal role of silanol nest in anchoring and maintaining the stability of PdOx nanoparticles on these zeolites. Theoretical calculations revealed a robust binding energy between PdOx nanoparticles and silanol nests, thus contributing to the outstanding durability of Pd/S-1-OH catalysts in harsh hydrothermal conditions. These findings are highly relevant for the design of highly stable Pd/zeolite catalysts, which holds significant importance in the field of heterogeneous catalysis.

CRediT authorship contribution statement

Yingjie Wang: Methodology, Investigation, Formal analysis, Writing original draft, Writing - review & editing. **Yanwei Sun:** Data curation, Investigation, Writing - review & editing. **Guangyan Xu:** Conceptualization, Methodology, Validation, Writing - review & editing, Project administration. **Zhi Liu:** Formal analysis, Validation. **Wei Shi:** Data curation, Investigation. **Xiaoyan Shi:** Formal analysis, Validation. **Yunbo Yu:** Formal analysis, Validation. **Hong He**: Conceptualization, Writing - review & editing, Project administration, Supervision.

Declaration of Competing Interest

The authors declare that they have no known competing financial interests or personal relationships that could have appeared to influence the work reported in this paper.

Data availability

Data will be made available on request.

Appendix A. Supplementary material

Additional experimental procedures/data are provided in the Supplementary Information: Detail information of experimental procedures, HR-TEM images, XRD patterns, H2-TPR profiles, O2-TPD profiles, XPS spectra, 1H NMR spectra, FTIR spectra, *in situ* Raman spectra, CH4-TPR and O2-TPO profiles, etc. (PDF)

Appendix A. Supporting information

Supplementary data associated with this article can be found in the online version at doi:10.1016/j.apcatb.2024.124221.

References

[1] Y.Q. Dai, P. Lu, Z.M. Cao, C.T. Campbell, Y.N. Xia, The physical chemistry and materials science behind sinter-resistant catalysts, Chem. Soc. Rev. 47 (2018) 4314–4331.
[2] E.D. Goodman, J.A. Schwalbe, M. Cargnello, Mechanistic Understanding and the Rational Design of Sinter-Resistant Heterogeneous Catalysts, ACS Catal. 7 (2017) 7156–7173.
[3] P. Gélin, M. Primet, Complete oxidation of methane at low temperature over noble metal based catalysts: a review, Appl. Catal. B 39 (2002) 1–37.
[4] A. Huonder, D. Olsen, Methane Emission Reduction Technologies for Natural Gas Engines: A Review, Energies 16 (2023) 7054–7072.
[5] P. Lott, M. Casapu, J.-D. Grunwaldt, O. Deutschmann, A review on exhaust gas after-treatment of lean-burn natural gas engines – From fundamentals to application, Appl. Catal. B 340 (2024) 123241–123278.
[6] A.W. Petrov, D. Ferri, F. Krumeich, M. Nachtegaal, J.A. van Bokhoven, O. Krocher, Stable complete methane oxidation over palladium based zeolite catalysts, Nat. Commun. 9 (2018) 2545–2553.
[7] M. Cargnello, J.J.D. Jaen, J.C.H. Garrido, K. Bakhmutsky, T. Montini, J.J.C. Gamez, R.J. Gorte, P. Fornasiero, Exceptional Activity for Methane Combustion over Modular Pd@CeO2 Subunits on Functionalized Al2O3, Science 337 (2012) 713–717.
[8] E.D. Goodman, A.C. Johnston-Peck, E.M. Dietze, C.J. Wrasman, A.S. Hoffman, F. Abild-Pedersen, S.R. Bare, P.N. Plessow, M. Cargnello, Catalyst deactivation via decomposition into single atoms and the role of metal loading, Nat. Catal. 2 (2019) 748–755.
[9] J.Y. Yang, M. Peng, G.Q. Ren, H.F. Qi, X. Zhou, J. Xu, F. Deng, Z.Q. Chen, J. C. Zhang, K.P. Liu, X.L. Pan, W. Liu, Y. Su, W.Z. Li, B.T. Qiao, D. Ma, T. Zhang, A Hydrothermally Stable Irreducible Oxide-Modified Pd/MgAl2O4 Catalyst for Methane Combustion, Angew. Chem. Int. Ed. 59 (2020) 1–6.
[10] S. Chen, S. Li, R. You, Z. Guo, F. Wang, G. Li, W. Yuan, B. Zhu, Y. Gao, Z. Zhang, H. Yang, Y. Wang, Elucidation of Active Sites for CH4 Catalytic Oxidation over Pd/CeO2 Via Tailoring Metal-Support Interactions, ACS Catal. 11 (2021) 5666–5677.
[11] X. Yang, Q. Li, E. Lu, Z. Wang, X. Gong, Z. Yu, Y. Guo, L. Wang, Y. Guo, W. Zhan, J. Zhang, S. Dai, Taming the stability of Pd active phases through a compartmentalizing strategy toward nanostructured catalyst supports, Nat. Commun. 10 (2019) 1611–1620.
[12] H. Xiong, D. Kunwar, D. Jiang, C.E. García-Vargas, H. Li, C. Du, G. Canning, X. I. Pereira-Hernandez, Q. Wan, S. Lin, S.C. Purdy, J.T. Miller, K. Leung, S.S. Chou, H.H. Brongersma, R. ter Veen, J. Huang, H. Guo, Y. Wang, A.K. Datye, Engineering catalyst supports to stabilize PdOx two-dimensional rafts for water-tolerant methane oxidation, Nat. Catal. 4 (2021) 830–839.
[13] H.M. Duan, R. You, S.T. Xu, Z.R. Li, K. Qian, T. Cao, W.X. Huang, X.H. Bao, Pentacoordinated Al3+-Stabilized Active Pd Structures on Al2O3-Coated Palladium Catalysts for Methane Combustion, Angew. Chem. Int. Ed. 58 (2019) 12043–12048.
[14] K. Murata, Y. Mahara, J. Ohyama, Y. Yamamoto, S. Arai, A. Satsuma, The Metal-Support Interaction Concerning the Particle Size Effect of Pd/Al2O3 on Methane Combustion, Angew. Chem. Int. Ed. 56 (2017) 15993–15997.
[15] J.J. Chen, Y. Wu, W. Hu, P.F. Qu, G.C. Zhang, P. Granger, L. Zhong, Y.Q. Chen, New insights into the role of Pd-Ce interface for methane activation on monolithic supported Pd catalysts: A step forward the development of novel PGM Three-Way Catalysts for natural gas fueled engines, Appl. Catal. B 264 (2020) 118576–118487.
[16] C. Chen, Y.H. Yeh, M. Cargnello, C.B. Murray, P. Fornasiero, R.J. Gorte, Methane Oxidation on Pd@ZrO2/SiAl2O3 Is Enhanced by Surface Reduction of ZrO2, ACS Catal. 4 (2014) 3902–3909.
[17] T.M. Onn, S.Y. Zhang, L. Arroyo-Ramirez, Y.C. Chung, G.W. Graham, X.Q. Pan, R. J. Gorte, Improved Thermal Stability and Methane-Oxidation Activity of Pd/Al2O3 Catalysts by Atomic Layer Deposition of ZrO2, ACS Catal. 5 (2015) 5696–5701.
[18] E.J. Jang, J. Lee, D.G. Oh, J.H. Kwak, CH4 Oxidation Activity in Pd and Pt-Pd Bimetallic Catalysts: Correlation with Surface PdOx Quantified from the DRIFTS Study, ACS Catal. 11 (2021) 5894–5905.
[19] Z. Hou, L. Dai, J. Deng, G. Zhao, L. Jing, Y. Wang, X. Yu, R. Gao, X. Tian, H. Dai, D. Wang, Y. Liu, Electronically Engineering Water Resistance in Methane Combustion with an Atomically Dispersed Tungsten on PdO Catalyst, Angew. Chem. Int. Ed. 61 (2022) e202201655.
[20] I. Friberg, N. Sadokhina, L. Olsson, The effect of Si/Al ratio of zeolite supported Pd for complete CH4 oxidation in the presence of water vapor and SO2, Appl. Catal. B 250 (2019) 117–131.
[21] A.W. Petrov, D. Ferri, O. Kröcher, J.A. van Bokhoven, Design of Stable Palladium-Based Zeolite Catalysts for Complete Methane Oxidation by Postsynthesis Zeolite Modification, ACS Catal. 9 (2019) 2303–2312.
[22] K. Khivantsev, N.R. Jaegers, L. Kovarik, M. Wang, J.Z. Hu, Y. Wang, M. A. Derewinski, J. Szanyi, The superior hydrothermal stability of Pd/SSZ-39 in low temperature passive NOx adsorption (PNA) and methane combustion, Appl. Catal. B 280 (2021) 119449–119459.
[23] J. Zhang, L. Wang, B.S. Zhang, H.S. Zhao, U. Kolb, Y.H. Zhu, L.M. Liu, Y. Han, G. X. Wang, C.T. Wang, D.S. Su, B.C. Gates, F.S. Xiao, Sinter-resistant metal nanoparticle catalysts achieved by immobilization within zeolite crystals via seed-directed growth, Nat. Catal. 1 (2018) 540–546.
[24] N. Wang, Q. Sun, R. Bai, X. Li, G. Guo, J. Yu, Situ Confinement of Ultrasmall Pd Clusters within Nanosized Silicalite-1 Zeolite for Highly Efficient Catalysis of Hydrogen Generation, J. Am. Chem. Soc. 138 (2016) 7484–7487.
[25] T. Li, A. Beck, F. Krumeich, L. Artiglia, M.K. Ghosalya, M. Roger, D. Ferri, O. Kröcher, V. Sushkevich, O.V. Safonova, J.A. van Bokhoven, Stable Palladium Oxide Clusters Encapsulated in Silicalite-1 for Complete Methane Oxidation, ACS Catal. 11 (2021) 7371–7382.
[26] C. Gao, F. Lyu, Y. Yin, Encapsulated Metal Nanoparticles for Catalysis, Chem. Rev. 121 (2021) 834–881.
[27] T.L. Cui, W.Y. Ke, W.B. Zhang, H.H. Wang, X.H. Li, J.S. Chen, Encapsulating Palladium Nanoparticles Inside Mesoporous MFI Zeolite Nanocrystals for Shape-Selective Catalysis, Angew. Chem. Int. Ed. 55 (2016) 9178–9182.
[28] W. Wang, W. Zhou, W. Li, X. Xiong, Y. Wang, K. Cheng, J. Kang, Q. Zhang, Y. Wang, In-situ confinement of ultrasmall palladium nanoparticles in silicalite-1 for methane combustion with excellent activity and hydrothermal stability, Appl. Catal. B 276 (2020) 119142–119151.
[29] Y. Sun, G. Xu, Y. Wang, W. Shi, Y. Yu, H. He, In Situ Synthesis of Encapsulated Pd@silicalite-2 for Highly Stable Methane Catalytic Combustion, Environ. Sci. Technol. 57 (2023) 20370–20379.

[30] H.-Y. Chen, J. Lu, J.M. Fedeyko, A. Raj, Zeolite supported Pd catalysts for the complete oxidation of methane: A critical review, Appl. Catal., A 633 (2022), 118534–118547.

[31] Q. Dai, Q. Zhu, Y. Lou, X. Wang, Role of Brønsted acid site during catalytic combustion of methane over PdO/ZSM-5: Dominant or negligible? J. Catal. 357 (2018) 29–40.

[32] Q. Li, Y. Wang, W. Si, Y. Peng, J. Li, Novel Insights on the Metal-Support Interactions of Pd/ZrO2 Catalysts on CH4 Oxidation, ACS Appl. Mater. Interfaces 15 (2023) 7959–7968.

[33] R. Ryoo, J. Kim, C. Jo, S.W. Han, J.C. Kim, H. Park, J. Han, H.S. Shin, J.W. Shin, Rare-earth-platinum alloy nanoparticles in mesoporous zeolite for catalysis, Nature 585 (2020) 221–224.

[34] I.C. Medeiros-Costa, E. Dib, N. Nesterenko, J.P. Dath, J.P. Gilson, S. Mintova, Silanol defect engineering and healing in zeolites: opportunities to fine-tune their properties and performances, Chem. Soc. Rev. 50 (2021) 11156–11179.

[35] Y. Liu, Z. Liu, Y. Hui, L. Wang, J. Zhang, X. Yi, W. Chen, C. Wang, H. Wang, Y. Qin, L. Song, A. Zheng, F.S. Xiao, Rhodium nanoparticles supported on silanol-rich zeolites beyond the homogeneous Wilkinson's catalyst for hydroformylation of olefins, Nat. Commun. 14 (2023) 2531–2540.

[36] G. Kresse, J. Furthmüller, Efficiency of ab-initio total energy calculations for metals and semiconductors using a plane-wave basis set, Comput. Mater. Sci. 6 (1996) 15–50.

[37] P.E. Blöchl, O. Jepsen, O.K. Andersen, Improved tetrahedron method for Brillouin-zone integrations, Phys. Rev. B 49 (1994) 16223–16233.

[38] R. Sajiv Kumar, R.E. Hayes, N. Semagina, Effect of support on Pd-catalyzed methane-lean combustion in the presence of water: Review, Catal. Today 382 (2021) 82–95.

[39] P. Velin, F. Hemmingsson, A. Schaefer, M. Skoglundh, K.A. Lomachenko, A. Raj, D. Thompsett, G. Smedler, P.-A. Carlsson, Hampered PdO Redox Dynamics by Water Suppresses Lean Methane Oxidation over Realistic Palladium Catalysts, ChemCatChem 13 (2021) 3765–3771.

[40] W. Huang, A.C. Johnston-Peck, T. Wolter, W.-C.D. Yang, L. Xu, J. Oh, B.A. Reeves, C. Zhou, M.E. Holtz, A.A. Herzing, A.M. Lindenberg, M. Mavrikakis, M. Cargnello, Steam-created grain boundaries for methane C-H activation in palladium catalysts, Science 373 (2021) 1518–1523.

[41] J. Chen, K. Giewont, E.A. Walker, J. Lee, Y. Niu, E.A. Kyriakidou, Cobalt-Induced PdO Formation in Low-Loading Pd/BEA Catalysts for CH4 Oxidation, ACS Catal. (2021) 13066–13076.

[42] Y. Lou, J. Ma, W. Hu, Q. Dai, L. Wang, W. Zhan, Y. Guo, X.-M. Cao, Y. Guo, P. Hu, G. Lu, Low-Temperature Methane Combustion over Pd/H-ZSM-5: Active Pd Sites with Specific Electronic Properties Modulated by Acidic Sites of H-ZSM-5, ACS Catal. 6 (2016) 8127–8139.

[43] J.B. Lim, D. Jo, S.B. Hong, Palladium-exchanged small-pore zeolites with different cage systems as methane combustion catalysts, Appl. Catal. B 219 (2017) 155–162.

[44] X.L. Zou, Z.B. Rui, H.B. Ji, Core-Shell NiO@PdO Nanoparticles Supported on Alumina as an Advanced Catalyst for Methane Oxidation, ACS Catal. 7 (2017) 1615–1625.

[45] R. Gholami, K.J. Smith, Activity of PdO/SiO2 catalysts for CH4 oxidation following thermal treatments, Appl. Catal. B (2015) 168–169, 156-163.

[46] A.H. Habibi, R.E. Hayes, N. Semagina, Evaluation of hydrothermal stability of encapsulated PdPt@SiO2 catalyst for lean CH4 combustion, Appl. Catal., A 556 (2018) 129–136.

[47] K. Murata, J. Ohyama, Y. Yamamoto, S. Arai, A. Satsuma, Methane Combustion over Pd/Al2O3 Catalysts in the Presence of Water: Effects of Pd Particle Size and Alumina Crystalline Phase, ACS Catal. 10 (2020) 8149–8156.

[48] X. Chen, Y. Cheng, C.Y. Seo, J.W. Schwank, R.W. McCabe, Aging, re-dispersion, and catalytic oxidation characteristics of model Pd/Al2O3 automotive three-way catalysts, Appl. Catal. B 163 (2015) 499–509.

[49] K. Okumura, S. Matsumoto, N. Nishiaki, M. Niwa, Support effect of zeolite on the methane combustion activity of palladium, Appl. Catal. B 40 (2003) 151–159.

[50] J. Xu, L. Ouyang, W. Mao, X.-J. Yang, X.-C. Xu, J.-J. Su, T.-Z. Zhuang, H. Li, Y.-F. Han, Operando and Kinetic Study of Low-Temperature, Lean-Burn Methane Combustion over a Pd/γ-Al2O3 Catalyst, ACS Catal. 2 (2012) 261–269.

[51] M. Van den Bossche, H. Gronbeck, Methane Oxidation over PdO(101) Revealed by First-Principles Kinetic Modeling, J. Am. Chem. Soc. 137 (2015) 12035–12044.

[52] Y. Zhang, Y. Cai, Y. Guo, H. Wang, L. Wang, Y. Lou, Y. Guo, G. Lu, Y. Wang, The effects of the Pd chemical state on the activity of Pd/Al2O3 catalysts in CO oxidation, Catal. Sci. Technol. 4 (2014) 3973–3980.

[53] Y. Ryou, J. Lee, S.J. Cho, H. Lee, C.H. Kim, D.H. Kim, Activation of Pd/SSZ-13 catalyst by hydrothermal aging treatment in passive NO adsorption performance at low temperature for cold start application, Appl. Catal. B 212 (2017) 140–149.

[54] T.M. Lardinois, J.S. Bates, H.H. Lippie, C.K. Russell, J.T. Miller, H.M. Meyer, K. A. Unocic, V. Prikhodko, X. Wei, C.K. Lambert, A.B. Getsoian, R. Gounder, Structural Interconversion between Agglomerated Palladium Domains and Mononuclear Pd(II) Cations in Chabazite Zeolites, Chem. Mater. 33 (2021) 1698–1713.

[55] J. Lee, Y. Ryou, S.J. Cho, H. Lee, C.H. Kim, D.H. Kim, Investigation of the active sites and optimum Pd/Al of Pd/ZSM-5 passive NO adsorbers for the cold-start application: Evidence of isolated-Pd species obtained after a high-temperature thermal treatment, Appl. Catal. B 226 (2018) 71–82.

[56] A. Toso, S. Colussi, S. Padigapaty, C. de Leitenburg, A. Trovarelli, High stability and activity of solution combustion synthesized Pd-based catalysts for methane combustion in presence of water, Appl. Catal. B 230 (2018) 237–245.

[57] C. He, Q. Shen, M. Liu, Toluene destruction over nanometric palladium supported ZSM-5 catalysts: influences of support acidity and operation condition, J. Porous Mater. 21 (2014) 551–563.

[58] Z. Liu, G. Xu, L. Zeng, W. Shi, Y. Wang, Y. Sun, Y. Yu, H. He, Anchoring Pt-doped PdO nanoparticles on highly dispersed La sites to create a methane oxidation catalyst, Appl. Catal. B 324 (2023) 122259–122268.

[59] M. Danielis, S. Colussi, C. de Leitenburg, L. Soler, J. Llorca, A. Trovarelli, Outstanding Methane Oxidation Performance of Palladium-Embedded Ceria Catalysts Prepared by a One-Step Dry Ball-Milling Method, Angew. Chem. Int. Ed. 57 (2018) 10212–10216.

[60] W. Shi, G. Xu, X. Han, Y. Wang, Z. Liu, S. Xue, N. Sun, X. Shi, Y. Yu, H. He, Nano-sized alumina supported palladium catalysts for methane combustion with excellent thermal stability, J. Environ. Sci. 126 (2023) 333–347.

[61] T. Karbowiak, M.A. Saada, S. Rigolet, A. Ballandras, G. Weber, I. Bezverkhyy, M. Soulard, J. Patarin, J.P. Bellat, New insights in the formation of silanol defects in silicalite-1 by water intrusion under high pressure, Phys. Chem. Chem. Phys. 12 (2010) 11454–11466.

[62] C.E. Bronnimann, R.C. Zeigler, G.E. Maciel, Proton NMR Study of Dehydration of the Silica Gel Surface, J. Am. Chem. Soc. 110 (1988) 2023–2026.

[63] C. Xiao, Y. Du, L. Dong, X. Zhou, Y. Xie, Z. Tan, PdOx/Silicalite-1 Catalyst Prepared by Room Temperature Ozone Treatment: Preparation Chemistry and Catalytic Performance for Methane Combustion, Catal. Lett. 147 (2017) 1775–1782.

[64] K. Yamagishi, S. Namba, T. Yashima, Defect Sites In Highly Siliceous HZSM-5 Zeolites: A Study Performed by Alumination and IR Spectroscopy, J. Phys. Chem. 95 (1991) 872–877.

[65] A. Zecchina, S. Bordiga, G. Spoto, L. Marchese, Silicalite Characterization. 1. Structure, Adsorptive Capacity, and IR Spectroscopy of the Framework and Hydroxyl Modes, J. Phys. Chem. 96 (1992) 4985–4990.

[66] Y. Wu, S. Holdren, Y. Zhang, S.C. Oh, D.T. Tran, L. Emdadi, Z. Lu, M. Wang, T. J. Woehl, M. Zachariah, Y. Lei, D. Liu, Quantification of rhenium oxide dispersion on zeolite: Effect of zeolite acidity and mesoporosity, J. Catal. 372 (2019) 128–141.

[67] A. Martinelli, S. Creci, S. Vavra, P.A. Carlsson, M. Skoglundh, Local anisotropy in single crystals of zeotypes with the MFI framework structure evidenced by polarised Raman spectroscopy, Phys. Chem. Chem. Phys. 22 (2020) 1640–1654.

[68] J. Zhang, Y. Chu, X. Liu, H. Xu, X. Meng, Z. Feng, F.-S. Xiao, Interzeolite transformation from FAU to CHA and MFI zeolites monitored by UV Raman spectroscopy, Chin. J. Catal. 40 (2019) 1854–1859.

[69] J. Ma, Y. Lou, Y. Cai, Z. Zhao, L. Wang, W. Zhan, Y. Guo, Y. Guo, The relationship between the chemical state of Pd species and the catalytic activity for methane combustion on Pd/CeO2, Catal. Sci. Technol. 8 (2018) 2567–2577.

[70] S. Bordiga, P. Ugliengo, A. Damin, C. Lamberti, G. Spoto, A. Zecchina, G. Spanò, R. Buzzoni, L. Dalloro, F. Rivetti, Hydroxyls nests in defective silicalites and strained structures derived upon dehydroxylation: vibrational properties and theoretical modelling, Top. Catal. 15 (2001) 43–52.

[71] A. Zecchina, S. Bordiga, G. Spoto, L. Marchese, Silicalite Characterization. 2. IR Spectroscopy of the Interaction of CO with Internal and External Hydroxyl Groups, J. Phys. Chem. 96 (1992) 4991–4997.

[72] H. Hattori, P. Arudra, A. Abdalla, A.M. Aitani, S.S. Al-Khattaf, Infrared Study of Silanol Groups on Dealuminated High Silica MFI Zeolite to Correlate Different Types of Silanol Groups with Activity for Conversion of 1-Butene to Propene, Catal. Lett. 150 (2019) 771–780.

[73] Y.H. Chin, C. Buda, M. Neurock, E. Iglesia, Consequences of metal-oxide interconversion for C-H bond activation during CH4 reactions on Pd catalysts, J. Am. Chem. Soc. 135 (2013) 15425–15442.

[74] A. Li, Y. Zhang, C.J. Heard, K. Golabek, X. Ju, J. Cejka, M. Mazur, Encapsulating Metal Nanoparticles into a Layered Zeolite Precursor with Surface Silanol Nests Enhances Sintering Resistance, Angew. Chem. Int. Ed. 62 (2023) e202213361.

[75] H. Xu, P. Liu, W. Zhang, Q. Wang, Y. Yang, Structure, stability, electronic and magnetic properties of monometallic Pd, Pt, and bimetallic Pd-Pt core-shell nanoparticles, Chem. Phys. 539 (2020) 110953–110964.

[76] O. Gantassi, C. Menakbi, N. Derbel, H. Guesmi, T. Mineva, Density Functional Study of Pd13 Magnetic Isomers in Gas-Phase and on (100)-TiO2 Anatase, J. Phys. Chem. C 119 (2015) 3153–3162.

[77] Y.H. Chin, C. Buda, M. Neurock, E. Iglesia, Reactivity of chemisorbed oxygen atoms and their catalytic consequences during CH4-O2 catalysis on supported Pt clusters, J. Am. Chem. Soc. 133 (2011) 15958–15978.

[78] L. Liu, J. Lu, Y. Yang, W. Ruettinger, X. Gao, M. Wang, H. Lou, Z. Wang, Y. Liu, X. Tao, L. Li, Y. Yang, H. Li, H. Zhou, C. Wang, Q. Luo, H. Wu, K. Zhang, J. Ma, X. Cao, L. Wang, F.-S. Xiao, Dealuminated Beta zeolite reverses Ostwald ripening for durable copper nanoparticle catalysts, Science 383 (2024) 94–101.

[79] D. Li, L. Wang, Y. Lu, H. Deng, Z. Zhang, Y. Wang, Y. Ma, T. Pan, Q. Zhao, Y. Shan, X. Shi, J. Ma, H. He, New insights into the catalytic mechanism of VOCs abatement over Pt/Beta with active sites regulated by zeolite acidity, Appl. Catal. B 334 (2023) 122811–122824.

[80] G. Brunklaus, H. Koller, S.I. Zones, Defect Models of As-Made High-Silica Zeolites: Clusters of Hydrogen-Bonds and Their Interaction with the Organic Structure-Directing Agents Determined from 1H Double and Triple Quantum NMR Spectroscopy, Angew. Chem. Int. Ed. 55 (2016) 14459–14463.

[81] C. Schroeder, C. Mück-Lichtenfeld, L. Xu, N.A. Grosso-Giordano, A. Okrut, C.-Y. Chen, S.I. Zones, A. Katz, M.R. Hansen, H. Koller, A Stable Silanol Triad in the Zeolite Catalyst SSZ-70, Angew. Chem. Int. Ed. 59 (2020) 10939–10943.

[82] S.V. Konnov, F. Dubray, E.B. Clatworthy, C. Kouvatas, J.P. Gilson, J.P. Dath, D. Minoux, C. Aquino, V. Valtchev, S. Moldovan, S. Koneti, N. Nesterenko, S. Mintova, Novel Strategy for the Synthesis of Ultra-Stable Single-Site Mo-ZSM-5 Zeolite Nanocrystals, Angew. Chem. Int. Ed. 59 (2020) 19553–19560.

[83] H.Y. Luo, L. Bui, W.R. Gunther, E. Min, Y. Román-Leshkov, Synthesis and Catalytic Activity of Sn-MFI Nanosheets for the Baeyer-Villiger Oxidation of Cyclic Ketones, ACS Catal. 2 (2012) 2695–2699.